



Article

Remote Sensing-Based Assessment of Evapotranspiration Patterns in a UNESCO World Heritage Site Under Increasing Water Competition

Maria C. Moyano ¹, Monica Garcia ², Luis Juana ¹ , Laura Recuero ^{3,4}, Lucia Tornos ¹, Joshua B. Fisher ⁵ , Néstor Fernández ^{6,7} and Alicia Palacios-Orueta ^{1,3,*}

- ¹ Departamento de Ingeniería Agroforestal, ETSIAAB, Universidad Politécnica de Madrid, Av. Puerta de Hierro, nº 2—4, Ciudad Universitaria, 28040 Madrid, Spain; mariacarmen.moyano@upm.es (M.C.M.)
- ² Estación Experimental de Zonas Áridas (EEZA-CSIC), La Cañada de San Urbano s/n, 04120 Almería, Spain
- ³ Centro de Estudios e Investigación para la Gestión de Riesgos Agrarios y Medioambientales (CEIGRAM), Universidad Politécnica de Madrid, C/Senda del Rey 13, 28040 Madrid, Spain; laura.recuero@upm.es
- ⁴ Departamento de Economía Agraria, Estadística y Gestión de Empresas, ETSIAAB, Universidad Politécnica de Madrid (UPM), Av. Puerta de Hierro, nº 2—4, Ciudad Universitaria, 28040 Madrid, Spain
- ⁵ Schmid College of Science and Technology, Chapman University, 1 University Drive, Orange, CA 92866, USA; jbfisher@chapman.edu
- ⁶ German Centre for Integrative Biodiversity Research (iDiv), Halle-Jena-Leipzig. Puschstraße. 4, 04103 Leipzig, Germany
- ⁷ Institute of Biology, Martin Luther University Halle-Wittenberg, Am Kirchtor 1, 06108 Halle (Saale), Germany
- * Correspondence: alicia.palacios@upm.es

Abstract

In water-scarce regions, natural ecosystems and agriculture increasingly compete for limited water resources, intensifying stress during periods of drought. To assess these competing demands, we applied a modified PT-JPL model that incorporates the thermal inertial approach as a substitute for relative humidity (*RH*) in estimating soil evaporation—a method that significantly outperforms the original PT-JPL formulation in Mediterranean semi-arid irrigated areas. This remote sensing framework enabled us to quantify spatial and temporal variations in water use across both natural and agricultural systems within the UNESCO World Heritage site of Doñana. Our analysis revealed an increasing evapotranspiration (*ET*) trend in intensified agricultural areas and rice fields surrounding the National Park ($R = 0.3$), contrasted by a strong negative *ET* trend in wetlands ($R < -0.5$). These opposing patterns suggest a growing diversion of water toward irrigation at the expense of natural ecosystems. The impact was especially marked during droughts, such as the 2011–2016 period, when precipitation declined by 16%. In wetlands, *ET* was significantly correlated with precipitation ($R > 0.4$), highlighting their vulnerability to reduced water inputs. These findings offer crucial insights to support sustainable water management strategies that balance agricultural productivity with the preservation of ecologically valuable systems under mounting climatic and anthropogenic pressures typical of semi-arid Mediterranean environments.

Keywords: evapotranspiration; remote sensing; PT-JPL; thermal; trends; drought; Doñana



Academic Editors: Yuanwei Qin,
Jun Zhai and Wei Cao

Received: 28 February 2025

Revised: 19 June 2025

Accepted: 27 June 2025

Published: 8 July 2025

Citation: Moyano, M.C.; Garcia, M.; Juana, L.; Recuero, L.; Tornos, L.; Fisher, J.B.; Fernández, N.; Palacios-Orueta, A. Remote Sensing-Based Assessment of Evapotranspiration Patterns in a UNESCO World Heritage Site Under Increasing Water Competition. *Remote Sens.* **2025**, *17*, 2339. <https://doi.org/10.3390/rs17142339>

Copyright: © 2025 by the authors.

Licensee MDPI, Basel, Switzerland.

This article is an open access article distributed under the terms and conditions of the Creative Commons Attribution (CC BY) license (<https://creativecommons.org/licenses/by/4.0/>).

1. Introduction

The growing global population and rising food demand is placing increasing pressure on natural ecosystems, many of which depend on the same water resources as agricultural lands [1–4]. Climate change is intensifying these challenges. The increasing frequency

and severity of extreme weather events, such as droughts, floods, and heatwaves, are threatening crop production and food security worldwide [5–7]. These climatic extremes not only disrupt agricultural productivity but also impair the functionality of ecosystems globally, underscoring the urgent need for adaptive strategies to safeguard both food security and ecosystem health [7,8].

A prime example of this is the Mediterranean region [9–11]. The Iberian Peninsula is projected to be one of the regions in the world most severely impacted by droughts [12,13] and as a result, competition for water resources is expected to intensify significantly [14]. These effects will be especially acute in the river basins of southern Spain [15], where irrigated agriculture accounts for 80% of total water extraction [16]. In the Guadalquivir River basin in southern Spain, water consumption is expected to increase up to 20% by 2050 [17], a trend that could further compromise the ecological integrity of dependent natural ecosystems [18]. A significant case within this basin is the Doñana Biosphere reserve located at the river's mouth and protected under multiple international frameworks, including the Ramsar Convention on Wetlands.

Given the projected decrease in precipitation across southern Europe and the Mediterranean basin, including the Guadalquivir River basin [19,20], there is an urgent need to understand how natural ecosystems respond to meteorological drivers—particularly precipitation—under increasingly arid conditions [21,22]. In regions like Doñana, where ecosystems are already sensitive to water availability, declining rainfall is expected to exacerbate existing stressors. These include intensive agricultural irrigation and groundwater abstraction, which further reduce water accessibility for wetlands and other natural habitats [23,24]. Understanding ecosystem responses to climatic variability is critical for anticipating tipping points, identifying thresholds, and informing adaptive water management strategies. Such strategies must account for both natural climate fluctuations and increasing anthropogenic pressures [25,26], which further constrain water availability for wetlands and other natural habitats [23].

This urgency is underscored by recent hydrological observations in the Doñana region, which reveal that streamflow rates have nearly halved and the water table has dropped by more than 6 m due to over-extraction, primarily for agriculture [27–29]. These changes are already placing considerable stress on the region's natural ecosystems, notably the wetlands. Recognizing the severity of the situation, the World Heritage Committee has called for a comprehensive assessment of Doñana's ecohydrological conditions to curb illegal water abstraction and prevent the site's designation as a World Heritage in Danger [30]. Since 2016, the Doñana area has been increasingly affected by anthropogenic pressures, such as intensified groundwater extraction, agricultural expansion, and policy changes, culminating in environmental and legal actions, including the European Commission's 2019 infringement procedure against Spain for non-compliance with the EU Habitats Directive (Case C-559/19) [31].

Providing scientific evidence through enhanced monitoring and accurate modeling of water use is essential for informing policymakers, supporting regulatory action, and adapting water demands to safeguard these threatened ecosystems [32].

A central component of this modeling effort is evapotranspiration (*ET*), which represents the largest water flux from land to atmosphere and is key to understanding historical and spatial dynamics of water consumption by both crops and natural vegetation [33,34]. Spatially distributed *ET* estimates are fundamental for quantifying historical water use patterns and for identifying critical areas of overuse or imbalance.

PT-JPL is a widely adopted model for estimating *ET* across diverse biomes and underpins NASA's ECOSTRESS mission [35]. However, it shows reduced accuracy in semi-arid agroecosystems, particularly due to its handling of soil evaporation (*ET*s) [36,37]. This

limitation stems from its reliance on the moisture content of the overlying atmosphere to simulate soil evaporation dynamics [38]. High values of vapor pressure deficit (*VPD*) may reflect the surrounding arid conditions but fail to capture fine-scale soil moisture dynamics, reducing *ET* reliability [39–43]. To address these shortcomings, remote sensing (RS)-based proxies, like apparent thermal inertia (ATI) and SWIR indices, have been integrated into PT-JPL [36,37,44], offering better spatial resolution and more direct sensitivity to surface moisture. PT-JPL-thermal is a modified version of the PT-JPL model [45], which incorporates thermal remote sensing data as a proxy to the soil moisture status, outperforming other RS models, such as the PM model adapted by Leuning et al. [46] and the MOD16 *ET* algorithm used by Mu et al. [47] and Mu et al. [48] in semi-arid regions. PT-JPL-thermal was benchmarked at EC flux sites [44] and later regionalized by Moyano et al. [49] to compare *VPD*-based approaches in semi-arid areas, validating ATI's effectiveness in capturing *ET* dynamics under Mediterranean conditions, specifically in Doñana.

Although several studies have analyzed *ET* dynamics within specific natural ecosystems of the Doñana region, such as wetlands, shrublands, and forested areas [23,50], there is still a lack of comprehensive, long-term assessments that integrate both the irrigated agricultural zones surrounding the park and the protected ecosystems within Doñana National Park. This gap in spatial integration and thematic scope has limited our understanding of the broader ecohydrological dynamics at the landscape scale and impedes the detection of regional water dynamics. In light of projected precipitation declines across the Mediterranean basin [21,22] and rising irrigation demands in the Guadalquivir River basin [51], it is increasingly important to assess how both natural and agricultural systems respond to meteorological drivers under growing anthropogenic pressures.

Simultaneous analysis of *ET* dynamics in relation to water use patterns across land use types, as well as its relationship with precipitation, can reveal areas of vulnerability, enhance understanding of ecosystem resilience, and support more adaptive and sustainable water resource planning, contributing to safer operating spaces for long-term conservation [27].

This study aims to quantify the spatio-temporal dynamics of evapotranspiration (*ET*) and assess the influence of meteorological drivers on water use across contrasting land systems in the UNESCO World Heritage Site of Doñana and its surrounding irrigated agricultural areas from 2003 to 2016. In this region, where water resources are increasingly contested between ecological conservation and intensive agriculture [52], comprehensive long-term assessments remain scarce. Notably, existing studies often overlook the integrated analysis of both the protected ecosystems within Doñana National Park and the adjacent agricultural zones, despite the area's critical ecological importance.

To achieve this goal, we set two specific objectives:

- To analyze the intra- and inter-annual dynamics of *ET* and the water deficit index (*WDI*) in the Doñana region, with a particular focus on differences between irrigated croplands and natural protected ecosystems within the park, while also examining the relationships between land cover types and meteorological drivers, especially precipitation.
- To assess the spatial patterns and temporal trends of *ET* and *WDI* over the study period, with special attention given to years of significant water stress, such as 2005, characterized by severe precipitation deficits affecting natural ecosystems, and 2007, when irrigation supply was notably insufficient.

2. Study Area and Data

2.1. Study Area

The study area covers Doñana National Park (54,251 ha) and the adjacent Natural Park (53,835 ha), located above the Almonte-Marismas aquifer in Andalusia, southern Spain

(36.98°N, 6.37°W). Within the park, the wetland landscape forms a mosaic of distinct types, including the seasonally flooded marshes, temporary dune ponds, and ecotone freshwater habitats lying between dunes and marshes [30]. These are complemented by shrublands and coniferous forests. Surrounding the protected areas are agriculturally developed lands, notably rice fields [18] along both banks of the Guadalquivir River and mixed irrigated croplands established on former marshland areas (Figure 1).

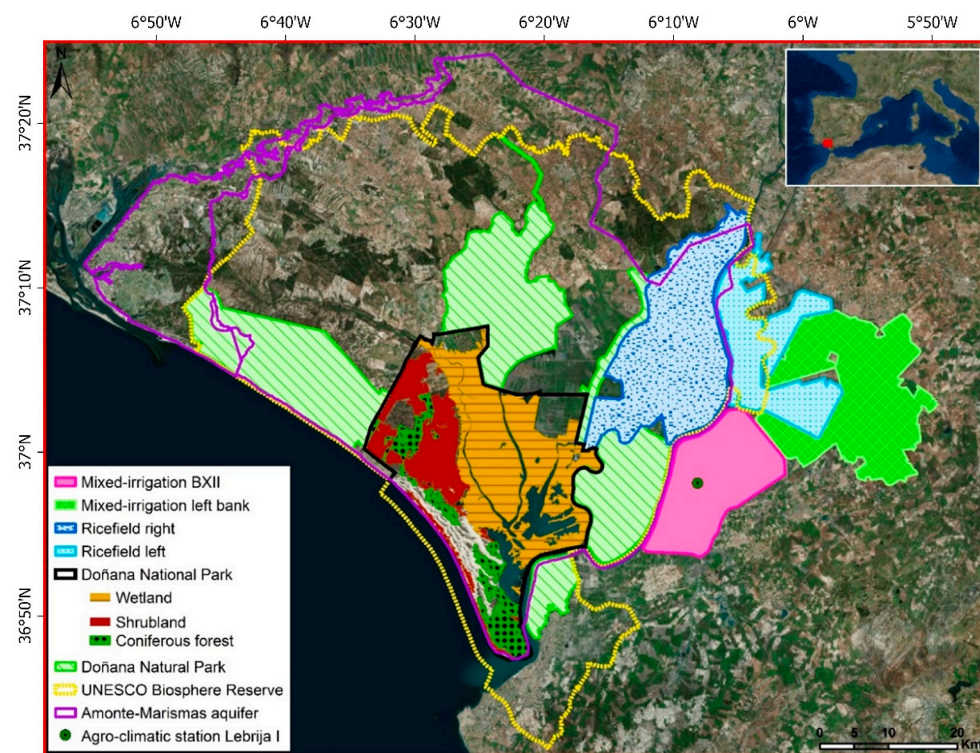


Figure 1. Map of the UNESCO protected study area and associated EU nitrate vulnerable zones in the region. The study area includes (i) irrigated areas: mixed-irrigation areas (BXII and left bank) and rice fields; (ii) natural ecosystems in the Doñana National Park: wetland, shrubland, and coniferous forest.

Historically, Doñana's marshes extended across approximately 150,000 ha, but have undergone substantial transformation over the last century [53]. Currently, only about 30,000 ha of seasonal marshes—fed by rainfall and surface streams—and 3000 ha of temporary dune ponds remain within the National Park. These ponds rely on the annual fluctuations of the Almonte-Marismas aquifer, which is nearly five times larger than the park itself [23,54]. The area is a crucial refuge for over half a million migratory birds and endangered species, including the Iberian lynx and the Spanish imperial eagle [55].

In the 1960s, the remaining ancient marshes were converted into arable land, causing a deep landscape change [52] and defining the actual landscape of the region. To counteract this trend, it was declared a National Park in 1969, included in the Ramsar Convention as one of the largest wetlands in Europe [28], and designated a World Heritage Site by UNESCO in 1995. The National Park has also been buffered by a Natural Park, which entered the endangered Montreux Record of Ramsar sites in 1990 [56].

In recent decades, a more gradual yet profound transformation has been reshaping the landscape of Doñana. The same groundwater that sustains the wetland's natural flooding cycles is increasingly being tapped for uses beyond the boundaries of the National Park.

Conflicts between environmental conservation and economic development in the Doñana region have grown significantly [53]. Since the 1970s, agricultural intensification and rising urban water demand have driven substantial groundwater extraction, leading to

historical drawdowns of up to 20 m in some areas [28,57]. This overexploitation threatens not only the long-term sustainability of the aquifer but also the stability of groundwater-dependent ecosystems, including ponds and marshes [23]. Given their strong reliance on groundwater, these wetlands are particularly vulnerable to fluctuations in aquifer levels. If the current management of the aquifer is continued over time, the sustainability of its associated ecosystems will be compromised [58]. Additionally, high concentrations of nitrates from agrarian origin in the aquifer [59] have led to many of the croplands, rice fields, and wetlands in the area to be designated as nitrate vulnerable zones [60] under the European Commission nitrates directive [61].

2.2. Remote Sensing Data

Multiple remote sensing observations were acquired from the Moderate Resolution Imaging Spectroradiometer (MODIS), using sensors from both the Aqua and Terra satellites. The satellite data were used in combination with in situ meteorological data (air temperature and radiation) as inputs for the PT-JPL-thermal model. MODIS land products were retrieved from the Earth Observing System Data and Information System (EOSDIS), a core capability in the National Aeronautics Space Administration (NASA) Earth Science Data Systems Program. All the selected MODIS products (version 5) were acquired at a 1 km pixel resolution for the 2003–2016 study period. The temporal resolutions of the data sets were (1) daily for the land surface temperature (LST), land emissivity (ϵ_s), and MODIS overpass time from MOD11A1 and MYD11A1, (2) 8-day composites of the land surface temperature (LST) from MOD11A2 and MYD11A2, (3) 8-day composites of the leaf area index (LAI) and fraction of photo-synthetically active radiation (f_{APAR}) from MOD15A2, as well as the broadband surface albedo (α) acquired from MCD43B3, and (4) 16-day composites of the normalized difference vegetation index ($NDVI$) retrieved from MOD13A2. To interpolate the daily values from the 8- and 16-day composite variables, each composite value was assumed to be constant over its respective period.

To ensure long-term consistency in the satellite data, all MODIS products used in this study were sourced from Collection 5 (version 5), which benefits from retrospective calibration and standardized processing algorithms across the full time series. We used data from both the Terra and Aqua platforms, enhancing temporal coverage and enabling cross-sensor consistency checks. While minor inconsistencies due to sensor degradation or algorithm updates cannot be entirely excluded, several measures were implemented to mitigate these effects. These include the application of product-specific quality control flags to retain only high-quality observations, and the integration of in situ meteorological data (air temperature and radiation) into the PT-JPL-thermal model, thereby reducing dependence on satellite-derived inputs alone.

2.3. Meteorological Data

Meteorological data were obtained from the agro-climatic station Lebrija I (36.98°N, 6.13°W, <https://www.juntadeandalucia.es/agriculturaypesca/ifapa/ria/>, (accessed on 15 June 2024)), which is a station site of the Agroclimatic Information Network of Andalusia (RIAA). This station is controlled by a CR10X datalogger with sensors to measure T_{air} (T_{max} , T_{min} , and T_{mean}), relative humidity (RH) (RH_{max} , RH_{min} , and RH_{mean}), solar radiation R_s , precipitation P , wind speed and direction, and reference evapotranspiration (ET_0) on a daily basis. The data are transferred by GSM modems for quality control and data validation [62].

2.4. Land Use Maps

Land use maps were retrieved from the 2013 update Land Cover and Use Information System of Spain (SIOSE) database in the Doñana region [63]. SIOSE is accessible at a

1:10,000 scale and follows the European Terrestrial Reference System 1989 (ETRS89) under the European Directive INSPIRE (2007/2/CE) requirements.

3. Methods

3.1. Remote Sensing ET Based on a Thermal and Optical RS Model

In this work, the PT-JPL-thermal model by García et al. [44], based on the approach by Fisher et al. [45], was spatially distributed over the study area for a 14 year-period at a daily time scale. The model was previously validated in the semi-arid region of Doñana and surrounding irrigated areas [49].

To facilitate comprehension of the model used in this work, all the equations and variables used to retrieve the *ET* as the combination of canopy transpiration and soil evaporation are detailed in Table 1.

Table 1. Equations and variables used to estimate the daily values of *ET* in the PT-JPL-thermal model. $\alpha_{PT} = 1.26$, the Priestley–Taylor coefficient; Δ is the slope of the saturation-to-vapor pressure curve (Pa K^{-1}); γ is the psychrometric constant (0.066 kPa C^{-1}); G is the soil heat flux (Wm^{-2}), negligible at the daily scale as in Fisher et al. [45]; $k_{RN} = 0.6$ [64]; LAI is from MOD15A2; σ is the Stefan–Boltzmann constant ($5.67 \times 10^{-8} \text{ Wm}^{-2}$); c and d are constants (0.261 and 7.77×10^{-4} , respectively); T_{max} and T_{min} ($^{\circ}\text{C}$) are the max and min climatic T_{air} [65]; N (h) is the time lag between sunrise and sunset (<https://www.esrl.noaa.gov/gmd/grad/researchp.html>, (accessed on 2 February 2020)); d is the time lag for the maximum temperature before sunset (1.86 h); *MODIS time* is the time from MYD11A1 or MOD11A1 depending on clouds; c is the time lag for the minimum air temperature after sunrise (-0.17 h); ϵ_S is the average of emissivity bands 31 and 32; *LST* is from MYD11A1 or MOD11A1 (depending on clouds); $R_{\downarrow S day}$ ($\text{MJ/m}^2/\text{day}$) is the climatic data [65]; α_{BSA} and α_{WSA} are the broadband black-sky and white-sky albedos; t (h) is the time lag between the sunrise time from NOAA and *MODIS time*; f_{APAR} is the fraction of absorbed photosynthetic active radiation; f_{IPAR} is the fraction of intercepted photosynthetic active radiation as a function of the *NDVI* acquired from MOD13A2 [42]; T_{opt} is the optimum temperature for plant growth (25°C) as in García et al. [44]; T_{am} is the daily mean T_{air} ($^{\circ}\text{C}$); (*LSTDay*–*LSTNight*) is the maximum daily *LST* oscillations from 8-day MYD11A2 and MOD11A2 data; θ is the latitude; and φ is the solar declination factor.

Variable Description	PT-JPL-Thermal Equations	Reference
Evapotranspiration	$ET = ET_c + ET_s$	[45]
Canopy transpiration	$ET_c = ET_{p_c} \cdot f_g \cdot f_m \cdot f_t$	[45]
Potential canopy transpiration	$ET_{p_c} = \alpha_{PT} \cdot \frac{\Delta}{\Delta + \gamma} \cdot (R_{nc} - G)$	[45]
• Net canopy radiation	$R_{nc} = R_n - R_{ns}$	[45]
• Net soil radiation	$R_{ns} = R_n \cdot e^{(-k_{RN} \cdot LAI)}$	[64]
• Net radiation	$R_n = R_L^{\downarrow} - R_L^{\uparrow} + R_S^{\downarrow} - R_S^{\uparrow} = R_L + R_S$	[45]
Instant. incoming longwave radiation	$R_{L_{inst}}^{\downarrow} = \sigma \cdot (T_{air_{MODIS-time}} + 273.15)^4 \cdot \left[1 - \left(c \cdot e^{(-d \cdot (T_{air_{MODIS-time}})^2)} \right) \right]$	[66]
Air temperature at MODIS _{pass-time}	$T_{air_{MODIS-time}} = (T_{max} - T_{min}) \cdot \sin\left(\frac{\pi \cdot m}{N + 2 \cdot d}\right) + T_{min}$	[67]
Number of hours from T_{min} until sunset	$m = MODIS_{time} - \left(12 - \left(\frac{N}{2}\right) + c\right)$	[67]
Instant. outgoing longwave radiation	$R_{L_{inst}}^{\uparrow} = -\epsilon_S \cdot \sigma \cdot T_S^4$	[68]
Daily shortwave radiation	$R_{S_{day}} = R_{S_{day}}^{\downarrow} \cdot (1 - \alpha)$	[68]
Albedo	$\alpha = 0.8 \cdot \alpha_{BSA} + 0.2 \cdot \alpha_{WSA}$	[69]

Table 1. Cont.

Variable Description	PT-JPL-Thermal Equations	Reference
Instant. shortwave radiation	$R_{S_{inst}} = \frac{R_{S_{day}}}{J} \cdot \frac{24}{N}$	[70]
Conversion factor day-inst	$J = \frac{2}{\sin\left(\frac{\pi \cdot t}{N}\right)}$	[70]
Instantaneous net radiation	$R_{n_{inst}} = R_{L_{inst}} + R_{S_{inst}}$	
Daily net radiation	$R_{n_{day}} = R_{n_{inst}} \cdot J \cdot \frac{N}{24}$	[71]
Canopy transpiration constraints		
• Green canopy fraction	$f_g = f_{APAR} / f_{IPAR}$	[45]
• Plant moisture constraint	$f_m = \frac{f_{APAR}}{f_{APAR_{max}}}$	[45]
• Plant temperature constraint	$f_t = 1.1814 / \left[\left(1 + e^{0.2 \cdot (T_{opt} - 10 - T_{am})} \right) \right] / \left[\left(1 + e^{0.3 \cdot (-T_{opt} - 10 + T_{am})} \right) \right]$	[68]
Soil evaporation	$ET_s = ET_p \cdot f_{sm}$	[45]
Potential soil evaporation	$ET_p = \alpha_{PT} \cdot \frac{\Delta}{\Delta + \gamma} \cdot (R_{ns} - G)$	[45]
Soil evaporation constraints		
• Soil moisture constraint	$f_{sm} = \frac{ATI - ATI_{min}}{ATI_{max} - ATI_{min}}$	[44]
Apparent thermal inertia	$ATI = C \cdot \frac{1 - \alpha}{(LST_{Day} - LST_{Night})}$	[44]
Solar flux correction factor	$C = \sin\theta \cdot \sin\varphi \cdot (1 - \tan^2\theta \cdot \tan^2\varphi) + \cos\theta \cdot \cos\varphi \cdot \arccos(-\tan\theta \cdot \tan\varphi)$	[72]

We calculated the daily *ET* derived from the PT-JPL-thermal model, as well as the water deficit index (*WDI*), defined as ET/ET_p [73], in the region on a pixel basis. ET_p was calculated as the aggregation of the potential evapotranspiration of the canopy and that of the soil (see Table 1).

The daily results obtained from the model over the period from 2003 to 2016 were spatially aggregated by land cover class, distinguishing between irrigated areas (including mixed-irrigation BXII, mixed-irrigation left bank, rice-right, and rice-left) and natural ecosystems (wetland, shrubland, and coniferous forest). For each class, we calculated the spatial mean of all constituent pixels on a daily basis.

3.2. Intra- and Inter-Annual Dynamics of Evapotranspiration in the Doñana Region and the Influence of Meteorological Drivers

Daily model outputs were aggregated to monthly and annual values at the pixel level to assess the *ET* and *WDI* intra-annual and inter-annual dynamics for all land cover classes.

To assess the inter-annual dynamics of *ET* and their relationship with meteorological drivers, particularly precipitation, standardized anomalies of precipitation $STDA_P$ and evapotranspiration $STDA_{ET}$ [74] for the period 2003–2016 were calculated (Equations (1) and (2)).

$$STDA_{P_i} = \frac{P_i - \bar{P}}{\sigma_P} \quad (1)$$

$$STDA_{ET_i} = \frac{ET_i - \bar{ET}}{\sigma_{ET}} \quad (2)$$

where P_i and ET_i represent the annual precipitation and evapotranspiration values for year i , \bar{P} and \bar{ET} are their respective time series averages, and σ_P and σ_{ET} are the respective standard deviations of the time series. The cumulative Gaussian distribution functions of the standardized anomalies $\Phi_{0,1}(STDA_{ET}, p)$ were used to indicate associated probability

levels. Values of $\Phi_{0,1}(STDA_{ET,p}) > 0.95$ and $\Phi_{0,1}(STDA_{ET,p}) < 0.05$ indicate significantly humid and dry years, respectively.

Finally, we calculated average intra-annual dynamics of *ET*, *NDVI*, and *WDI* over the study period, focusing on three years with contrasting moisture conditions: 2005 (anomalously dry), 2010 (anomalously wet), and 2007 (marked by notably low actual *ET* values in irrigated areas relative to the long-term mean), derived from the ($STDA_{ET,p}$) analysis.

3.3. Spatial Patterns of Evapotranspiration Dynamics Across Land Cover Types (2003–2016) and During Years of Significant Water Constraints

Pixel-based average values of *ET* and *WDI* were calculated for the full study period (2003–2016). Years with significant negative deviation over the average were identified as experiencing strong water-limited conditions, resulting from either meteorological drought (precipitation deficits) or hydrological stress related to water management practices.

For these years, we analyzed the spatial distribution of both *ET* and the water deficit index (*WDI*) by land cover class to explore differential ecosystem responses under water-limited conditions. This analysis allowed us to identify spatially differentiated responses across land cover types and assess their vulnerability to hydrological stress.

Finally, a pixel-level correlation analysis of the daily *ET* values over time was performed to evaluate the temporal *ET* trends of the various land cover types throughout the study period. This analysis was further refined by dividing the temporal data into multi-year intervals categorized as wetter or drier periods, with separate correlation analyses conducted for each.

4. Results

4.1. Intra- and Inter-Annual Dynamics of Evapotranspiration in the Doñana Region and the Influence of Meteorological Drivers

The daily *ET* time series derived from the PT-JPL-thermal model revealed clearly differentiated spatio-temporal patterns determined by the various land cover classes over the period spanning from 2003 to 2016.

In **natural ecosystems** (Figure 2a), the maximum average monthly *ET* values occurred during late spring and early summer. Specifically, the wetlands reached their peak *ET* in May (109 mm/month), the shrublands in June–July (98 mm/month), and the coniferous forests in July (180 mm/month). In the wetlands, the *WDI* values in May generally remained above 0.5, except in 2005 and 2012, when significant water deficits were recorded ($WDI < 0.25$). Decreasing *WDI* values were consistently observed from spring around April–May until the end of summer in September across the study period. In the shrublands, the July *WDI* values averaged 0.4 but dropped below 0.29 in 2005, reflecting intensified water stress during that year.

In the **irrigated areas** (Figure 2b), *ET* consistently peaked during the irrigation season (June–August), with July showing the highest values across the series—198 mm/month in rice fields and 125 mm/month in mixed-irrigation areas. During the years 2006 to 2008, although July remained the month with the maximum *ET*, we found a clear reduction compared to all the years in the study period. Specifically, *ET* in July dropped by up to 50% in rice fields and 30% in mixed-irrigation areas, standing out clearly within the time series. These reductions were also reflected in the *WDI* values: while summer *WDI* typically exceeded 0.8, indicating low water stress, the values fell below 0.5 in rice fields during this period. A similar trend was observed in mixed-irrigation areas, where the *WDI* decreased from the average 0.5 to 0.35 in 2008, suggesting marked deficit conditions during these peak *ET* months.

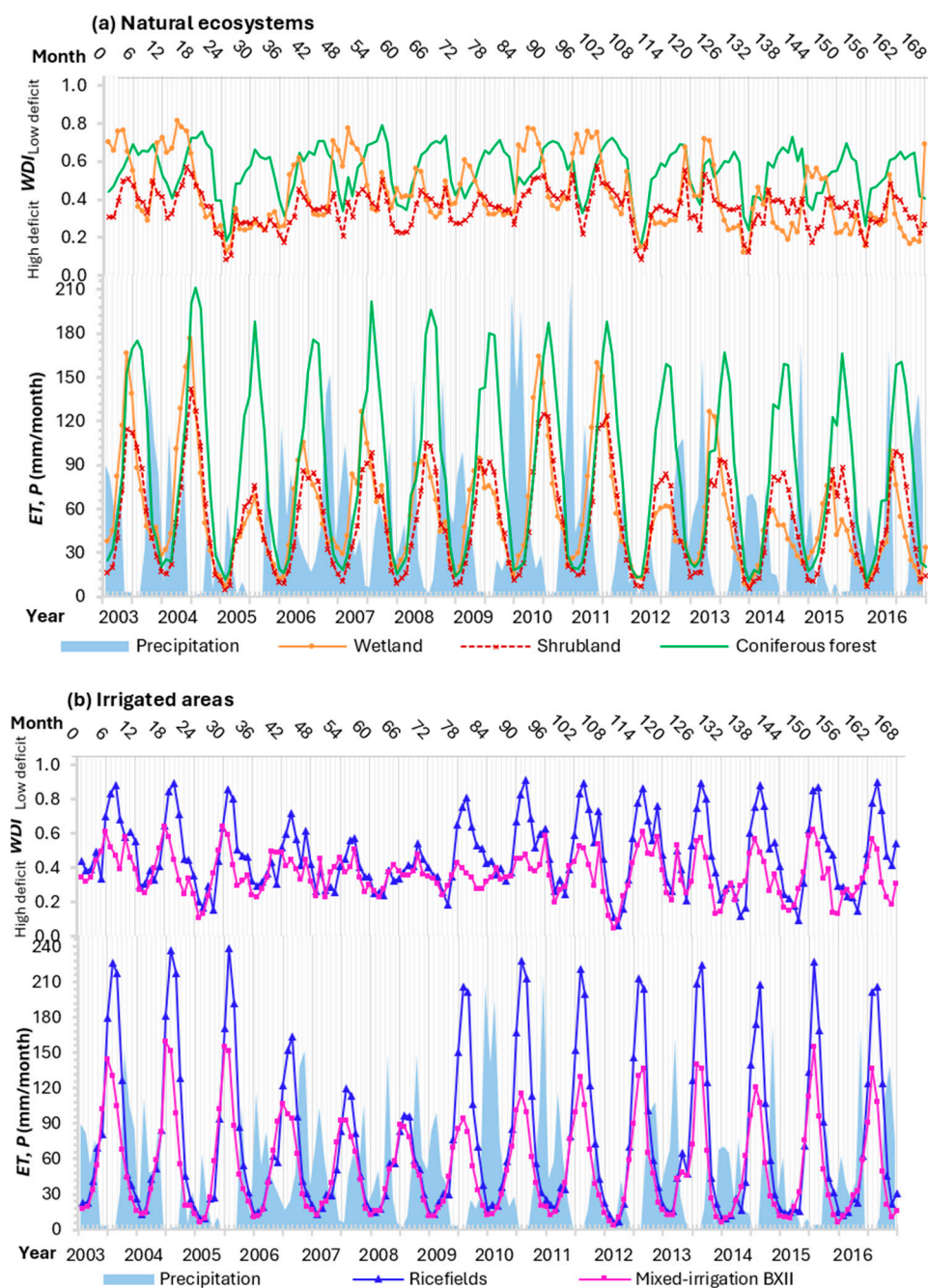


Figure 2. Monthly average values of ET (mm/month) and WDI (ET/ET_p) derived from the PT-JPL-thermal model are presented for (a) Doñana natural ecosystems (wetland, shrubland, and coniferous forest) and (b) the irrigated areas (mixed-irrigation and rice fields), as well as the monthly aggregates of daily precipitation (P) (mm/month) derived from the agro-climatic station Lebrija I (36.98°N lat., 6.13°W long) over the period from 2003 to 2016. Due to the strong similarity between the rice-right and rice-left areas, as well as between the mixed-irrigation BXII and mixed-irrigation left bank areas, only the rice-right and mixed-irrigation BXII areas are presented.

Secondly, we assessed the inter-annual dynamics of evapotranspiration and the WDI . To identify specific years in which these variables presented significant variations, the daily model results were aggregated to annual values per pixel and discretized by land cover class (Figure 3).

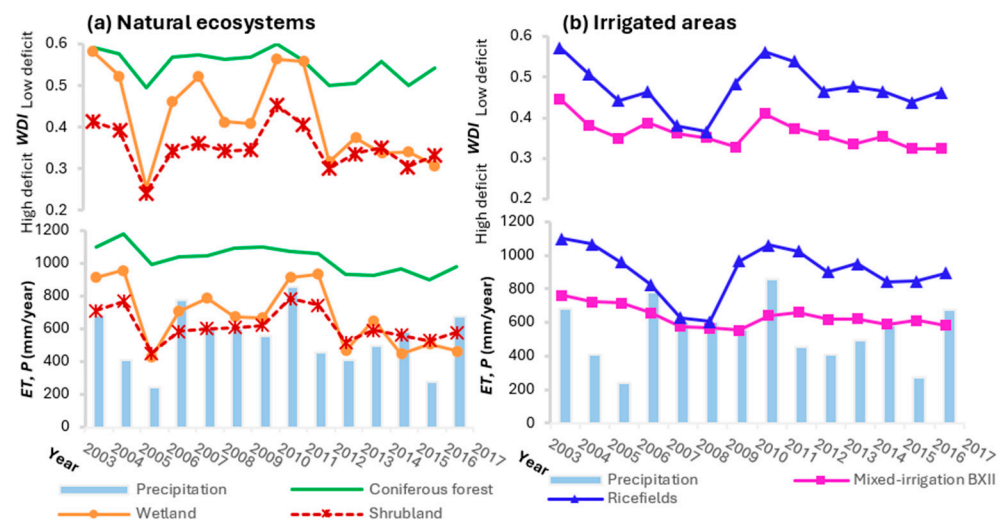


Figure 3. Annual average values of ET (mm/year) and WDI (ET/ET_p) derived from the PT-JPL-thermal model are presented for (a) Doñana natural ecosystems (wetland, shrubland, and coniferous forest) and (b) the irrigated areas (mixed-irrigation and rice fields) as well as annual aggregates of daily precipitation (P) (mm/month) derived from the agro-climatic station Lebrija I (36.98°N lat., 6.13°W long) over the period from 2003 to 2016. Due to the strong similarity between the rice-right and rice-left areas, as well as between the mixed-irrigation BXII and mixed-irrigation left bank areas, only the rice-right and mixed-irrigation BXII areas are presented.

In the **natural ecosystems**, the average annual values of ET over the period 2003–2016 reached 680 mm/year in the wetland, 620 mm/year in the shrubland, and 1020 mm/year in the coniferous forest. The lowest ET values were recorded in 2005, coinciding with the driest year (240 mm of annual precipitation), with 430 mm/year in the wetland and 450 mm/year in the shrubland. Persistently low ET values were also observed from 2011 to 2016, averaging 507 mm/year for the wetland and 550 mm/year for the shrubland. Regarding the WDI , the highest deficits were similarly observed in 2005 (0.25 for the wetland, 0.24 for the shrubland, and 0.49 for the coniferous forest), and during 2011–2016, when values remained below 0.33 for both the wetland and the shrubland, compared to their average annual WDI values of 0.43 and 0.35, respectively.

In the **irrigated areas**, the minimum ET values occurred in 2007 and 2008, reaching 605 mm/year in the rice fields and 530 mm/year in the mixed-irrigation sites, (compared to their respective long-term averages of 900 mm/year and 620 mm/year. During the period from 2007 to 2008, ET represented only 40% of potential evapotranspiration (ET_p) in all the irrigated areas, and the WDI values were notably low, averaging 0.38 in the rice fields compared to a long-term average of 0.47.

The $STDA_P$ analysis (Figure 4) showed that the year 2005 was anomalously dry, with $\Phi_{0,1}(STDA_P)$ values below -1.64 , corresponding to a probability of occurrence $P[STDA_P \leq -1.64] = 0.05$. The year 2010 was anomalously humid, with $\Phi_{0,1}(STDA_P)$ values over 1.64 , corresponding to a probability of occurrence $P[STDA_P \geq 1.64] = 0.05$.

We then compared these precipitation anomalies with corresponding ET anomalies, disaggregated by natural ecosystems and irrigated areas, to assess the influence of precipitation variability on ET dynamics. The analysis of $STDA_{ET}$ revealed distinct inter-annual patterns between natural ecosystems and irrigated areas.

In **natural ecosystems** (Figure 4a), the $STDA_{ET}$ values were generally positive from 2003 to 2011, suggesting stable or above-average ET conditions during this period, except in 2005, when $STDA_{ET}$ dropped close to -1.64 , corresponding to a substantial reduction in ET in wetlands and shrublands. From 2012 to 2016, the $STDA_{ET}$ values were predominantly negative, suggesting a consistent decline in ET .

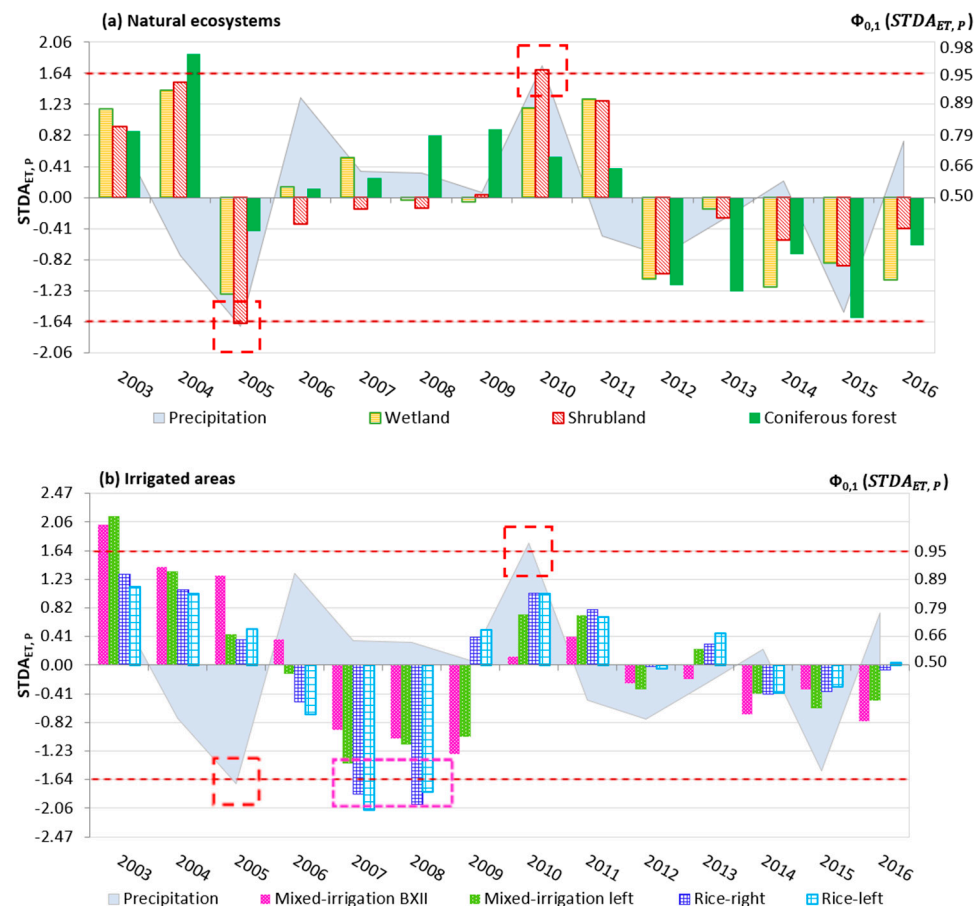


Figure 4. The annual standardized anomalies of evapotranspiration (ET) and corresponding cumulative distribution function $\Phi_{0,1}(STDA_{ET})$ in the secondary axis, discretized for (a) Doñana natural ecosystems, and (b) the irrigated areas, as well as the annual standardized anomalies of aggregated precipitation (P) and corresponding cumulative distribution function $\Phi_{0,1}(STDA_P)$ from 2003 to 2016. The red square indicates anomalous years derived from the standardized precipitation anomalies, corresponding to a probability of occurrence of $\Phi_{0,1}(STDA_P)$ below 5%. The pink square highlights anomalous years identified from the standardized anomalies of ET , corresponding to a probability of occurrence of $\Phi_{0,1}(STDA_{ET})$ below 5%.

In the **irrigated areas** (Figure 4b), the most pronounced anomalies were observed during 2007 and 2008, when rice fields showed $STDA_{ET}$ values below -1.64 , with marked low values in actual ET relative to the long-term mean.

The $STDA_{ET}$ patterns in natural ecosystems significantly mirrored those of the precipitation $STDA_P$, as illustrated in Figure 4a. To quantify this relationship, we performed a correlation analysis between the annually aggregated ET and precipitation P , disaggregated by land cover class. The results reveal a significant correlation in natural ecosystems, with coefficients exceeding $R > 0.4$ in both the wetland and shrubland. Conversely, no meaningful relationship was observed in the irrigated areas, where ET dynamics appeared largely decoupled from inter-annual variations in precipitation (Figure 4b).

Finally, we calculated the average intra-annual dynamics of ET , $NDVI$, and WDI over the study period, focusing on three years with contrasting moisture conditions: 2005 (anomalously dry), 2010 (anomalously wet), and 2007 (marked by notably low actual ET values in irrigated areas relative to the long-term mean) (Figure 5a,b).

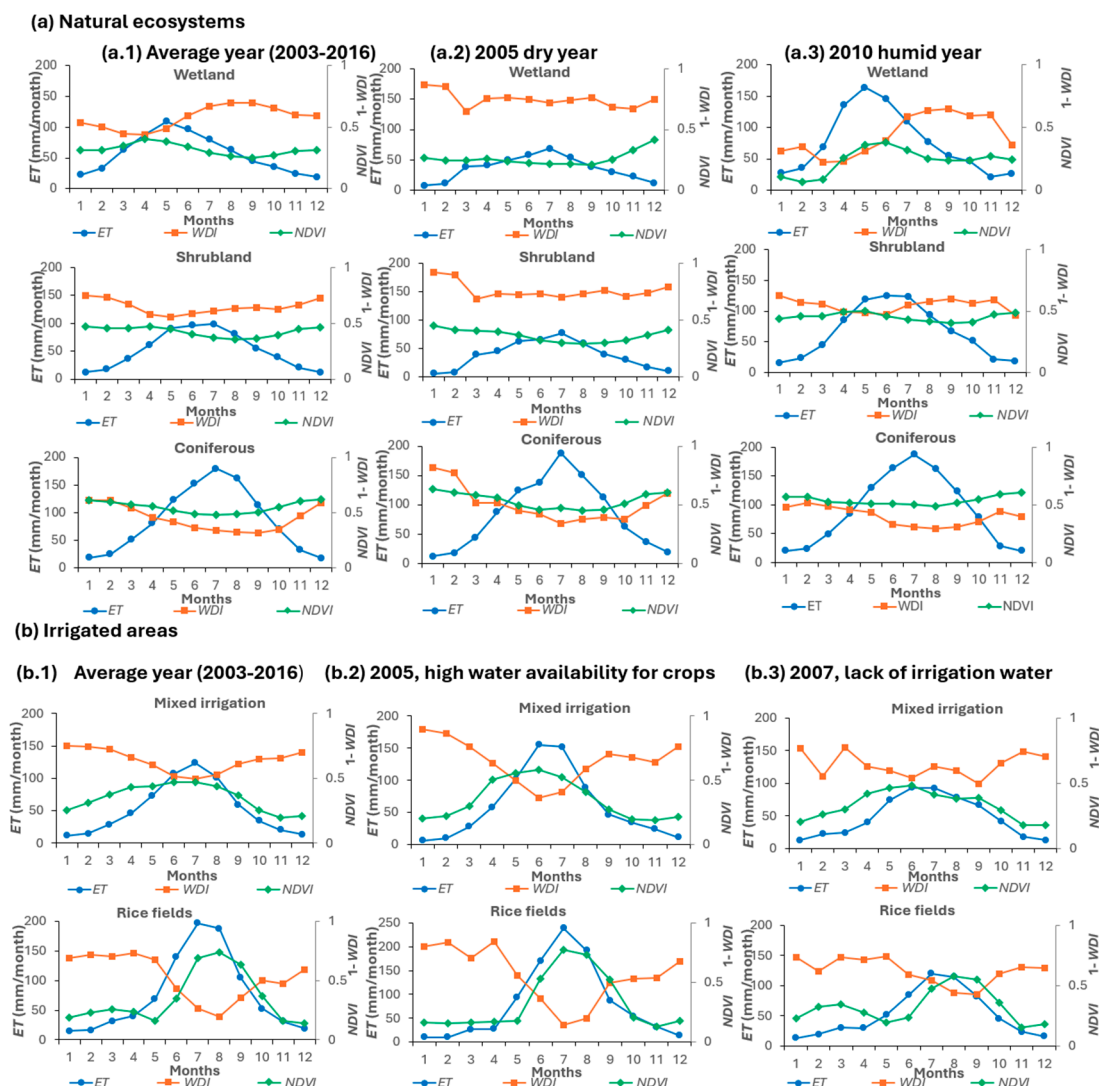


Figure 5. The average yearly values of ET (mm/month), WDI (ET/ET_p), and $NDVI$ (0–1) derived from the PT-JPL-thermal model over the period from 2003 to 2016 (a.1) as well as annual values for year 2005 (dry year) (a.2) and year 2010 (humid year) (a.3) are presented for (a) Doñana natural ecosystems (wetland, shrubland, and coniferous forest). The average yearly values of ET (mm/month), WDI (ET/ET_p), and $NDVI$ (0–1) derived from the PT-JPL-thermal model over the period from 2003 to 2016 (b.1) as well as annual values for year 2005 with high water availability for crops (b.2) and year 2007 with lack of irrigation water (b.3) are presented for (b) the irrigated areas (mixed-irrigation and rice fields). Due to the strong similarity between the rice-right and rice-left areas, as well as between the mixed-irrigation BXII and mixed-irrigation left bank areas, only the rice-right and mixed-irrigation BXII areas are presented.

In all land cover types except wetlands, the beginning of the year is characterized by high WDI values, mainly due to low temperatures and limited vegetative activity, as phenological development has not yet started. As temperatures rise in late winter and early spring, vegetation begins to transpire, gradually reducing the ET deficit.

4.2. Spatial Patterns and Trends of Evapotranspiration Across Land Cover Types (2003–2016) and During Years of Significant Water Constraints

To examine the spatial dynamics of ET and WDI under water-limited conditions across irrigated areas and natural ecosystems, we first calculated the average ET per pixel for the entire study period (2003–2016) to establish a reference baseline (Figure 6b). We then analyzed the years 2005 and 2007, each characterized by distinct water constraints affecting

different land systems. In 2005, the driest year of the period, with annual precipitation of 240 mm, natural ecosystems showed marked reductions in *ET* and lower *WDI* values (Figure 6c,d). In contrast, in 2007, limited water availability for irrigation, particularly in the rice fields, resulted in sharp *ET* declines and significantly reduced the *WDI* values in those zones (Figure 6e,f).

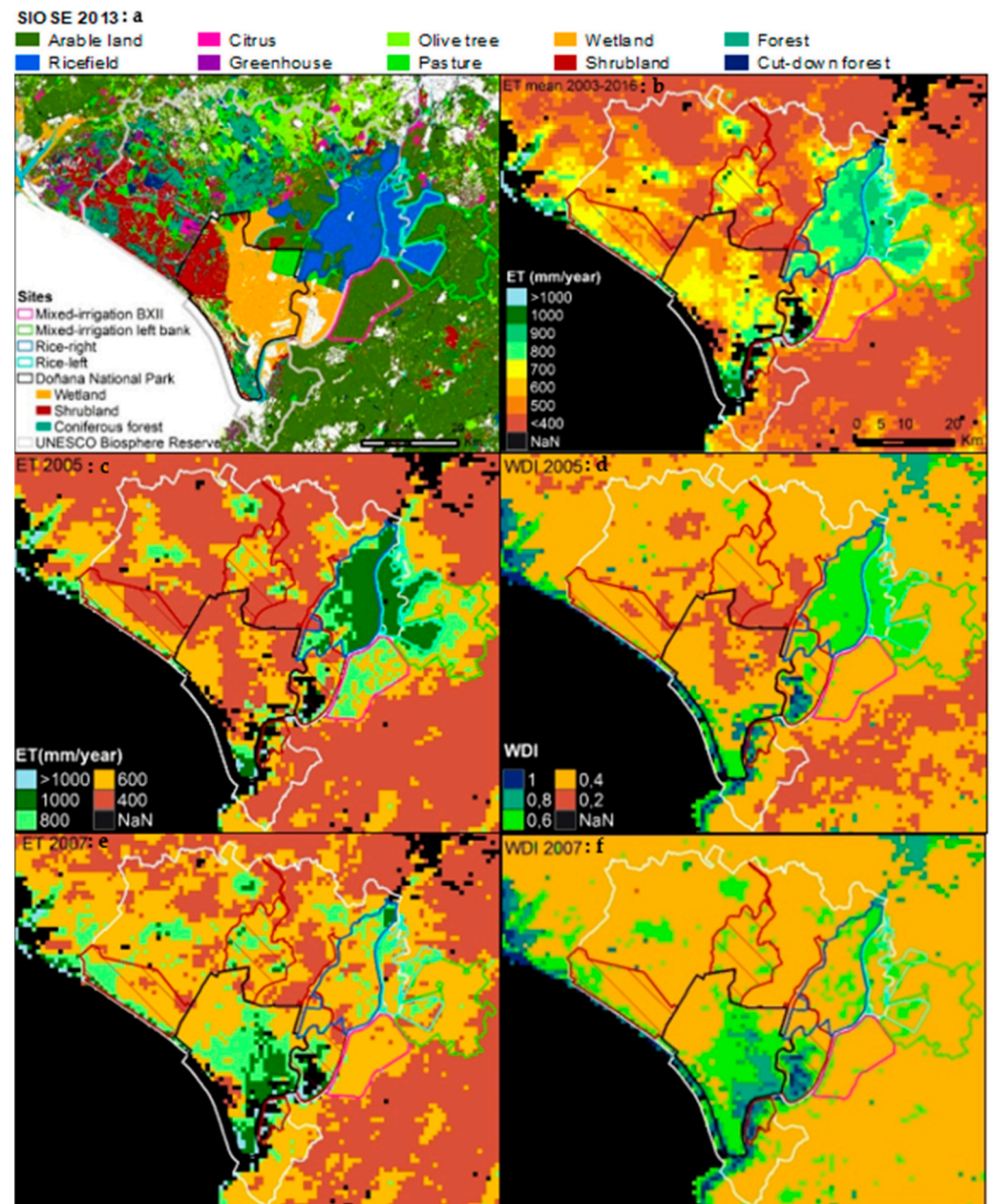


Figure 6. (a) Land use map of the Doñana region derived from the Spanish Land Occupation Information System (SIOSE). (b) The mean annual *ET* (mm/year) for the period 2003–2016, displayed on a pixel basis. (c) The *ET* distribution (mm/year) and (d) *WDI* values for 2005, the driest year in the study period (annual precipitation = 240 mm), highlighting substantial *ET* reductions in natural ecosystems. (e) The *ET* distribution (mm/year) and (f) *WDI* values for 2007, a year marked by reduced irrigation supply, showing pronounced *ET* declines in irrigated areas, particularly rice fields.

Finally, we performed a pixel-wise correlation analysis of the daily *ET* values over time to evaluate the temporal *ET* trends across various land cover types throughout the study period. The resulting correlation coefficients highlight distinct differences among the land cover categories (Figure 7b). The strongest negative correlations ($R < -0.5$) were

concentrated in natural ecosystems, particularly within the wetlands (indicated by red frames in Figure 7b). Conversely, positive trends were predominantly found in irrigated areas, with the highest coefficients (up to $R = 0.30$) observed in rice fields, the central zone of the western Natural Park, and scattered patches in the northwestern sector of the National Park (highlighted by blue frames in Figure 7b).

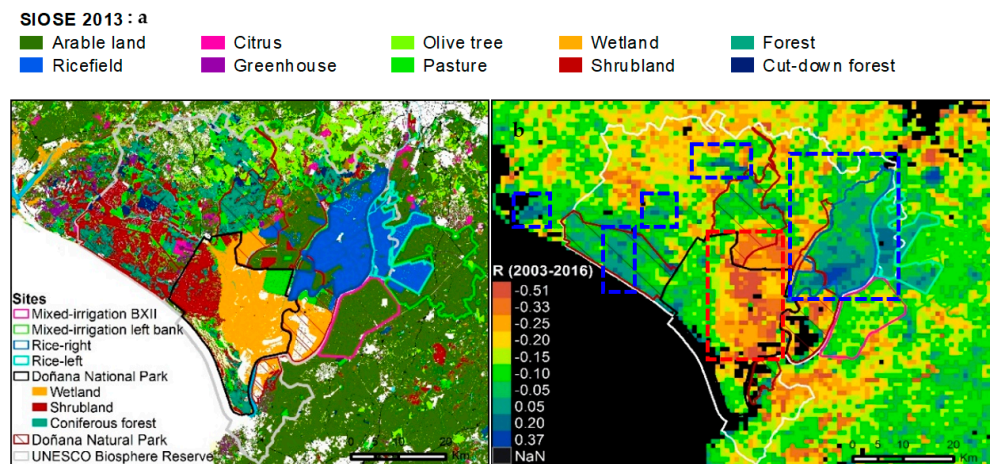


Figure 7. (a) Spanish Land Occupation Information System (SIOSE). (b) *ET* trends in the Doñana region over 2003–2016 expressed as the R correlation value between *ET* and time (in days). The red and blue squares represent the lowest (wetland areas) and highest (rice fields and various scattered patches across the Region) R values detected in the region. A positive correlation reflects an increasing trend in *ET* over time, while a negative correlation indicates a decreasing trend.

The pixel-wise correlation was further stratified by the prolonged wetter (2005–2011) and drier (2011–2016) periods identified in Figure 4. Irrigated areas were excluded from this analysis, as previous results (Figure 4b) indicate a lack of direct correspondence between *ET* and precipitation in those zones. The most notable shift in *ET* trends between the periods occurred in the wetlands, where the correlation values changed from positive ($R > 0.3$) during the wetter phase (Figure 8b) to strongly negative ($R < -0.5$) during the drier phase (Figure 8c). Shrubland and coniferous forest areas exhibited more moderate changes in *ET* trends between the two periods. This analysis highlights the varying degrees of ecosystem sensitivity to precipitation variability.

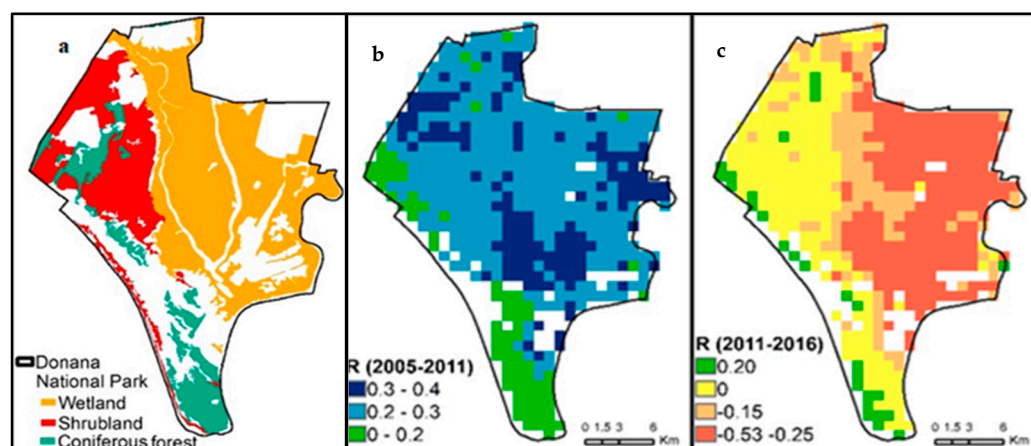


Figure 8. (a) Spanish Land Occupation Information System (SIOSE) for the Doñana National Park (wetland, shrubland, and coniferous forest). (b) *ET* trends in the natural ecosystems over the more humid period (2006–2011). (c) *ET* trends in the natural ecosystems over the drier period (2011–2016), expressed as the R correlation value between *ET* and time (in days). A positive correlation reflects an increasing trend in *ET* over time, while a negative correlation indicates a decreasing trend.

5. Discussion

In this study, we analyzed spatio-temporal monthly and annual evapotranspiration (*ET*) time series derived from the PT-JPL-thermal model for the period 2003–2016. This timeframe was selected to maintain consistency with prior applications of the PT-JPL-thermal model in the Doñana region, which were validated against in situ data up to 2012, showing strong agreement (ρ_1 month-lag = 0.94), as reported by Moyano et al. [49]. Extending the analysis to 2016 allowed us to capture a broader range of hydro-climatic variability beyond the validation period, including notable drought years, such as 2005 and 2015, which significantly impacted the Iberian Peninsula [75,76]. Incorporating more recent years would require additional validation efforts to ensure that the model remained accurate under increasingly altered land and water use regimes.

Significant differences in the temporal dynamics of *ET* and *WDI* were observed over the 2003–2016 study period, with distinct patterns emerging across different land cover types. Intra- and inter-annual dynamics provided key information to assess the importance of the balance between energy provision and water availability for *ET*, as well as the impact of droughts on the *ET* of different land covers.

The PT-JPL-thermal model effectively captured the diverse intra-annual *ET* dynamics of **natural ecosystems** over the study period, reflecting their varying capacities to access water, as previously reported by Moyano et al. [49]. These presented peak *ET* in early spring and summer (Figure 5a), with an average of 96 mm/month across wetlands, shrublands, and coniferous forests. Specifically, wetlands showed the highest *ET* fluxes and *NDVI* values in spring until April–May, indicating increased importance of vegetation transpiration, coinciding with post-rainfall water availability and the onset of vegetation growth. These dynamics align with previously reported intra-annual *ET* patterns by Drexler et al. [77]. In shrublands, peak *ET* occurs slightly later at the beginning of the summer, around June–July, while the *WDI* reaches its minimum, indicating water availability and vegetation growth conditions. As the season transitions into summer, the *NDVI* values decline slightly (Figure 5a), coinciding with reduced precipitation and increasing moisture deficits driven, consistent with observations in semi-arid shrublands by Nagler et al. [78]. For coniferous forests, the maximum *ET* was observed later in the summer, around July–August.

The analysis of monthly *ET* series over the study period in **the irrigated areas** revealed that the intra-annual *ET* dynamics derived from the PT-JPL-thermal model closely followed on-site irrigation management practices, with peak values occurring in the summer months and averaging 162 mm/month across rice fields and mixed-irrigation areas (Figure 2b). In mixed-irrigated areas in particular (Figure 5b), the maximum *ET*, peak *NDVI*, and minimum *WDI* typically aligned between June and August in years with sufficient water availability. Although rice fields share characteristics with wetlands due to the presence of standing water, they display distinct temporal dynamics. High *WDI* values were observed early in the year before field flooding, followed by a decline after crop establishment. During the initial growth phase, *ET* increases more rapidly than the *NDVI*, indicating a predominance of evaporation; both variables reach peak values around July, when evaporation and transpiration jointly contribute to the total *ET*. This strong alignment with irrigation practices underscores the effectiveness of using apparent thermal inertia (*ATI*) as a proxy for soil evaporation in the PT-JPL-thermal model, where replacing relative humidity (*RH*) with *ATI* significantly improves performance in semi-arid irrigated areas with active water management. As reported by Zhang et al. [38], even when driven by in situ *RH* measurements, the original PT-JPL model consistently underperforms in agroecosystems, an issue particularly evident in actively managed irrigated landscapes, as also noted by Marshall et al. [37]. Our findings support the value of thermal-based indicators for capturing spatial and temporal variability in soil moisture.

Figure 4 further illustrates the relationship between observed *ET* and precipitation patterns from 2003 to 2016, and additionally highlights years identified as anomalously dry, wet, or exhibiting significant deviations in *ET* dynamics.

In particular, the year 2005 was classified as anomalously dry (Figure 4a) and coincided with one of the most severe drought episodes recorded both globally and in the Iberian Peninsula [75].

The assessment of inter-annual *ET* variations in **natural ecosystems** revealed pronounced reductions in 2005 (Figure 3a), a year marked by severe drought conditions (Figure 4a). The extent of the impact varied by vegetation type, with wetlands being the most affected. In recent decades, the wetland has shifted from relying primarily on alluvial inputs to depending mainly on rainfall [50], leading to near-desiccation of ponds during dry years [79], especially in this region where precipitation is steadily decreasing [23,80]. *ET* in the wetland declined by up to 55%, accompanied by persistently low *NDVI* values, underscoring their strong dependence on precipitation. Additionally, intra-annual dynamics (Figure 5a) reveal that in 2005, the *ET* peak was delayed until July, compared to the usual April–May maximum. This shift suggests a diminished contribution from vegetation transpiration during that period. Shrublands experienced a 27% reduction in *ET*, while coniferous forests were largely unaffected. This ecosystem maintained relatively stable *ET* levels throughout the year, demonstrating greater resilience to drought conditions, possibly owing to their deep-rooted water access strategies (Figure 5a) [81]. These findings align with those of Garcia et al. [82], who also identified wetlands as the most sensitive to rainfall variability, with coniferous forests showing the highest resilience.

Regarding **irrigated areas**, no significant *ET* reduction was observed in 2005, Figure 3b, as these systems are less directly dependent on precipitation. In the irrigated areas, the effects of the 2005 drought manifested with a time lag, starting from 2007 (Figures 3b and 4b). Reservoir and groundwater reserves were heavily depleted in 2005, leading to insufficient water supplies for irrigation in the following hydrological years [80], and consequently causing significant *ET* reductions in irrigation-dependent areas. Irrigated areas exhibited notable *ET* decreases during the period from 2006 to 2008, with the most evaporative month, July, showing reductions up to 50% in rice fields and 30% in mixed-irrigation areas (Figures 2b and 5b) when compared to the officially recorded period between 2002 to 2005 [80].

The distinct impact of the 2005 drought across different land cover types is spatially illustrated in Figure 6c,d. Reddish-orange pixels indicate areas with the lowest *ET* values (<600 mm/year) and highest water deficits ($WDI < 0.4$), most notably within the wetlands. Conversely, greenish pixels represent areas with the highest *ET* values (around 900 mm/year) and lowest water deficits ($WDI > 0.6$), primarily corresponding to rice fields and coniferous forests, which were not immediately affected by the severe precipitation decline in 2005. As shown in Figure 6e, particularly for 2007, all areas cultivated with rice presented *ET* values of around 600 mm, even reaching minimum values up to 400 mm, very far from the average *ET* of 900 mm observed during the entire study period (Figure 6b). Similar patterns were found in *WDI* dynamics, with average values in the rice fields of around 0.4 (Figure 6f), much higher water deficits in comparison to those years not affected by irrigation restrictions.

In contrast to 2005, the year 2010 was identified as anomalously humid, with a probability of occurrence below 5% (Figure 4a,b). Particularly in the wetlands, which are highly dependent on precipitation, the *WDI* is lower at the beginning of the year (Figure 5a), suggesting that *ET* is predominantly driven by surface evaporation rather than plant transpiration. In these ecosystems, *ET* peaks in April–May, concurrently with the *NDVI*, indicating an increase in the importance of vegetation transpiration.

The model's sensitivity to ET variations due to precipitation constraints or irrigation restrictions is highly valuable in a context of increasing competition for water resources. Understanding how precipitation variability, together with its persistence in time and space, affects the behavior of vegetation and crops can help anticipate possible responses of ecosystems to climate-related restrictions [82] in contexts of increasing water competition.

Two marked pluri-annual periods of ET were observed in the natural ecosystems (Figure 4a), aligning with the corresponding pluri-annual periods of precipitation P . In particular, we distinguished a more humid period (2006–2011), with $STDA_P > 0$, and a drier period from 2011–2016, with $STDA_P < 0$. Focusing on discretized ET trends for the two pluri-annual periods distinguished in Figure 4, the most significant change in ET between periods corresponded indeed to the wetland, with R values decreasing from positive values of $R > 0.3$ over 2006 to 2011 (Figure 8b) to negative values of $R < -0.5$ from 2011 to 2016 (Figure 8c). This means a 35% ET reduction in the wetland between the two periods (from $ET = 775$ mm/year over 2006–2011 to $ET = 507$ over 2011–2016). Precipitation trends may partially explain ET reductions observed in the wetland. Indeed, precipitation P decreased from 576 mm/year over 2006–2011 to 487 mm/year over 2011–2016, which corresponds to a 16% reduction between the two periods, thus affecting the contributions of precipitation regimes to the wetland dynamics in the last years of the study series.

The results of the correlation analysis model over the entire period from 2003 to 2016 revealed significant positive ET trends ($R > 0.30$) in the rice fields and several patches in the northwest area of the National Park (Figure 7b), regions previously identified as undergoing agricultural intensification in recent years [83]. Conversely, negative ET trends were observed across the Doñana natural ecosystems, particularly pronounced in the wetland ($R < -0.43$). This decline is partly driven by land-use changes favoring more economically profitable activities, which have led to a drop in the aquifer's water table, posing a threat to the conservation of these natural ecosystems [32]. Unlicensed greenhouses cover over 6000 ha in the region, extracting groundwater through illegal wells [83]. In addition, Custodio et al. [84] estimated an average annual extraction of about 90 hm³, representing 45% of the aquifer's recharge. This over-extraction reduces groundwater contributions to streamflows feeding the wetland during summer months [83]. Particularly within the network of piezometers across the aquifer, the level of "Caracoles" in the wetland lowered from 1.4 to 2.6 m in the period of study from 2003 to 2016 [58]. Compounding this issue are projected declines in precipitation [85], which, as shown in Figure 4, have immediate adverse effects on natural ecosystems, particularly shallow-rooted wetlands.

In response to mounting challenges, the World Heritage Committee has called for urgent action to address groundwater over-extraction [86], aiming to preserve Doñana's unique ecosystems while promoting sustainable agricultural practices. This call to action comes amid escalating conflicts between environmental conservation and economic development in the region [52], where Doñana National Park remains a critical global biodiversity hotspot [29]. In this Mediterranean region, characterized by a mosaic of natural ecosystems and irrigated agricultural lands, the PT-JPL model has proven effective in assessing ET dynamics [58] in an area of rapid greenhouse expansion surrounding the Park [29], proving to be a sound tool to inform water management decisions aiming to equilibrate natural ecosystems and irrigation use.

The modeling framework presented in this study involves several sources of uncertainty that warrant consideration. First, precipitation inputs were obtained from a single meteorological station without spatial regionalization. While this ensures consistent temporal coverage, it may not fully represent spatial variability in rainfall, which is particularly important in heterogeneous landscapes, such as the Doñana region. Second, the daily values for variables derived from the 8- and 16-day MODIS composites were

interpolated, assuming that each composite value remained constant over its respective period. Although future studies could improve accuracy by integrating higher-resolution and spatially distributed meteorological data, the results presented here provide a robust representation of water use dynamics across contrasting land systems.

6. Conclusions

We assessed the evapotranspiration (*ET*) responses of natural ecosystems and irrigated lands in the Mediterranean Doñana region using the PT-JPL-thermal model. The daily *ET* spatio-temporal series revealed distinct and coherent patterns across land cover types. From 2003 to 2016, increased water use, indicated by positive *ET* trends ($R = 0.30$), was observed in rice fields and several zones in the northwestern area of Doñana National Park, corresponding to regions of intensified agriculture. In contrast, the strongest negative correlations ($R < -0.5$) were found in natural ecosystems, particularly within the wetland. The model clearly captured intra-annual dynamics and contrasting responses to wet and dry years, enabling robust differentiation of drought impacts and ecosystem behavior at seasonal scales. Persistent droughts had the greatest impact on wetlands, where *ET* and precipitation were strongly correlated ($R > 0.4$). In shrublands, the correlation was moderate, while in coniferous forests, it was not significant, likely due to deeper groundwater access during dry periods. The results align with independent sources, confirming the model's reliability in tracking water use over time. By jointly analyzing natural and irrigated systems, this study offers novel, spatially explicit insights into *ET* dynamics in Doñana. A key methodological innovation is the use of apparent thermal inertia (*ATI*) instead of relative humidity (*RH*) to estimate soil evaporation, providing a more robust and physically grounded proxy for monitoring *ET* in semi-arid and irrigated landscapes. These findings significantly advance our understanding of ecohydrological processes in Doñana and support more informed sustainable water management. They reinforce the World Heritage Committee's call by providing tools for improved monitoring, enabling more effective action to curb unsustainable water use and protect both agricultural and ecological values in this critical region.

Author Contributions: Conceptualization, M.C.M. and M.G.; Methodology, M.G. and L.T.; Software, M.C.M.; Validation, M.C.M. and J.B.F.; Formal analysis, M.C.M., M.G., L.J., L.R. and L.T.; Investigation, M.C.M., M.G. and N.F.; Resources, M.C.M.; Data curation, M.C.M. and M.G.; Writing—original draft, M.C.M.; Writing—review & editing, L.T., J.B.F. and N.F.; Visualization, M.C.M., L.J., and L.R.; Supervision, M.C.M., L.J. and A.P.-O.; Funding acquisition, M.C.M. and L.J. All authors have read and agreed to the published version of the manuscript.

Funding: This work was supported by the Spanish Centre for Hydrographic Studies (CEH-CEDEX), the European Cooperation on Science and Technology through the COST Action ES1106 AGRIWAT, and the FORWARD project under the ERA-NET Cofund WaterWorks2015 Call.

Data Availability Statement: The original remote sensing data used in the study are openly available at Earth Observing System Data and Information System (EOSDIS) at <https://www.earthdata.nasa.gov/about/esdis/eosdis>, accessed on 26 June 2025. Meteorological data used in this study are openly available at <https://www.juntadeandalucia.es/agriculturaypesca/ifapa/ria>, accessed on 26 June 2025.

Acknowledgments: This study was funded by the European Cooperation on Science and Technology (COST), under the COST Action ES1106 AGRIWAT, the Spanish Centre for Hydrographic Studies (CEDEX, Madrid), and the FORWARD project under the ERA-NET Cofund WaterWorks2015 Call. MODIS data were obtained through NASA's Earth Observing System Data and Information System EOSDIS (<https://reverb.echo.nasa.gov>, accessed on 26 June 2025). Climatic data were gathered from the IFAPA agro-climatic stations net, co-financed by the European Regional Development Fund

(ERDF). JBF was supported in part by NASA ECOSTRESS Science and Applications Team (ESAT) (80NSSC23K0309) and acknowledges support from the NSF Division of Earth Sciences (2012893) through CUAHSI and the USGS John Wesley Powell Center for Analysis and Synthesis.

Conflicts of Interest: The authors declare no conflict of interest.

References

1. Muller, A.; Schader, C.; El-Hage Scialabba, N.; Brüggemann, J.; Isensee, A.; Erb, K.-H.; Smith, P.; Klocke, P.; Leiber, F.; Stolze, M.; et al. Strategies for Feeding the World More Sustainably with Organic Agriculture. *Nat. Commun.* **2017**, *8*, 1290. [\[CrossRef\]](#)
2. Javadian, M.; Behrangi, A.; Smith, W.K.; Fisher, J.B. Global Trends in Evapotranspiration Dominated by Increases across Large Cropland Regions. *Remote Sens.* **2020**, *12*, 1221. [\[CrossRef\]](#)
3. Tanentzap, A.J.; Lamb, A.; Walker, S.; Farmer, A. Resolving Conflicts between Agriculture and the Natural Environment. *PLoS Biol.* **2015**, *13*, e1002242. [\[CrossRef\]](#)
4. Rastogi, M.; Kolur, S.M.; Burud, A.; Sadineni, T.; Sekhar, M.; Kumar, R.; Rajput, A. Advancing Water Conservation Techniques in Agriculture for Sustainable Resource Management: A Review. *J. Geogr. Environ. Earth Sci. Int.* **2024**, *28*, 41–53. [\[CrossRef\]](#)
5. Mushtaq, S.; White, N.; Cockfield, G.; Power, B.; Jakeman, G. Reconfiguring Agriculture through the Relocation of Production Systems for Water, Environment and Food Security under Climate Change. *J. Agric. Sci.* **2015**, *153*, 779–797. [\[CrossRef\]](#)
6. Sharma, T.; Vittal, H.; Karmakar, S.; Ghosh, S. Increasing Agricultural Risk to Hydro-Climatic Extremes in India. *Environ. Res. Lett.* **2020**, *15*, 34010. [\[CrossRef\]](#)
7. Scholes, R.J. Climate Change and Ecosystem Services. *Wiley Interdiscip. Rev. Clim. Change* **2016**, *7*, 537–550. [\[CrossRef\]](#)
8. Muluneh, M.G. Impact of Climate Change on Biodiversity and Food Security: A Global Perspective—A Review Article. *Agric. Food Secur.* **2021**, *10*, 36. [\[CrossRef\]](#)
9. Giorgi, F. Climate Change Hot-Spots. *Geophys. Res. Lett.* **2006**, *33*, L08707. [\[CrossRef\]](#)
10. Trambly, Y.; Llasat, M.C.; Randin, C.; Coppola, E. Climate Change Impacts on Water Resources in the Mediterranean. *Reg. Environ. Change* **2020**, *20*, 83. [\[CrossRef\]](#)
11. Rodriguez-Ramirez, N.; Santonja, M.; Baldy, V.; Ballini, C.; Montès, N. Shrub Species Richness Decreases Negative Impacts of Drought in a Mediterranean Ecosystem. *J. Veg. Sci.* **2017**, *28*, 985–996. [\[CrossRef\]](#)
12. Diffenbaugh, N.S.; Pal, J.S.; Giorgi, F.; Gao, X. Heat Stress Intensification in the Mediterranean Climate Change Hotspot. *Geophys. Res. Lett.* **2007**, *34*, L11706. [\[CrossRef\]](#)
13. Soares, P.M.M.; Careto, J.A.M.; Russo, A.; Lima, D.C.A. The Future of Iberian Droughts: A Deeper Analysis Based on Multi-Scenario and a Multi-Model Ensemble Approach. *Nat. Hazards* **2023**, *117*, 2001–2028. [\[CrossRef\]](#)
14. Hurtado, A.R.; Díaz-Cano, E.; Berbel, J. The Paradox of Success: Water Resources Closure in Axarquía (Southern Spain). *Sci. Total Environ.* **2024**, *946*, 174318. [\[CrossRef\]](#) [\[PubMed\]](#)
15. IPCC. *Climate Change 2014: Impacts, Adaptation, and Vulnerability. Part B: Regional Aspects. Contribution of Working Group II to the Fifth Assessment Report of the Intergovernmental Panel on Climate Change*; Barros, V.R., Field, C.B., Dokken, D.J., Mastrandrea, M.D., Mach, K.J., Bilir, T.E., Chatterjee, M., Ebi, K.L., Estrada, Y.O., Genova, R.C., et al., Eds.; Cambridge University Press: Cambridge, UK; New York, NY, USA, 2014.
16. Minacapilli, M.; Agnese, C.; Blanda, F.; Cammalleri, C.; Ciraolo, G.; D'Urso, G.; Iovino, M.; Pumo, D.; Provenzano, G.; Rallo, G. Estimation of Actual Evapotranspiration of Mediterranean Perennial Crops by Means of Remote-Sensing Based Surface Energy Balance Models. *Hydrol. Earth Syst. Sci.* **2009**, *13*, 1061–1074. [\[CrossRef\]](#)
17. Chavez-Jimenez, A.; Granados, A.; Garrote, L.; Martín-Carrasco, F. Adapting Water Allocation to Irrigation Demands to Constraints in Water Availability Imposed by Climate Change. *Water Resour. Manag.* **2015**, *29*, 1413–1430. [\[CrossRef\]](#)
18. García de Jalón, S.; Iglesias, A.; Cunningham, R.; Pérez Díaz, J.I. Building Resilience to Water Scarcity in Southern Spain: A Case Study of Rice Farming in Doñana Protected Wetlands. *Reg. Environ. Change* **2014**, *14*, 1229–1242. [\[CrossRef\]](#)
19. Andrade, C.; Contente, J.; Santos, J.A. Climate Change Projections of Aridity Conditions in the Iberian Peninsula. *Water* **2021**, *13*, 2035. [\[CrossRef\]](#)
20. Lorenzo, M.N.; Alvarez, I. Climate Change Patterns in Precipitation over Spain Using CORDEX Projections for 2021–2050. *Sci. Total Environ.* **2020**, *723*, 138024. [\[CrossRef\]](#)
21. Moss, W.E.; Crausbay, S.D.; Rangwala, I.; Wason, J.W.; Trauernicht, C.; Stevens-Rumann, C.S.; Sala, A.; Rottler, C.M.; Pederson, G.T.; Miller, B.W.; et al. Drought as an Emergent Driver of Ecological Transformation in the Twenty-First Century. *Bioscience* **2024**, *74*, 524–538. [\[CrossRef\]](#)
22. Zhang, L.; Deng, C.; Kang, R.; Yin, H.; Xu, T.; Kaufmann, H.J. Assessing the Responses of Ecosystem Patterns, Structures and Functions to Drought under Climate Change in the Yellow River Basin, China. *Sci. Total Environ.* **2024**, *929*, 172603. [\[CrossRef\]](#) [\[PubMed\]](#)

23. de Felipe, M.; Aragonés, D.; Díaz-Paniagua, C. Thirty-Four Years of Landsat Monitoring Reveal Long-Term Effects of Groundwater Abstractions on a World Heritage Site Wetland. *Sci. Total Environ.* **2023**, *880*, 163329. [CrossRef] [PubMed]
24. Naranjo-Fernández, N.; Guardiola-Albert, C.; Aguilera, H.; Serrano-Hidalgo, C.; Rodríguez-Rodríguez, M.; Fernández-Ayuso, A.; Ruiz-Bermudo, F.; Montero-González, E. Relevance of Spatio-Temporal Rainfall Variability Regarding Groundwater Management Challenges under Global Change: Case Study in Doñana (SW Spain). *Stoch. Environ. Res. Risk Assess.* **2020**, *34*, 1289–1311. [CrossRef]
25. Frietsch, M.; Loos, J.; Löhr, K.; Sieber, S.; Fischer, J. Future-Proofing Ecosystem Restoration Through Enhancing Adaptive Capacity. *Commun. Biol.* **2023**, *6*, 377. [CrossRef] [PubMed]
26. Naderi, L.; Karamidehkordi, E.; Badsar, M.; Moghadas, M. Impact of Climate Change on Water Crisis and Conflicts: Farmers' Perceptions at the Zayandeh Rud Basin in Iran. *J. Hydrol. Reg. Stud.* **2024**, *54*, 101878. [CrossRef]
27. Green, A.J.; Alcorlo, P.; Peeters, E.T.; Morris, E.P.; Espinar, J.L.; Bravo-Utrera, M.A.; Bustamante, J.; Díaz-Delgado, R.; Koelmans, A.A.; Mateo, R.; et al. Creating a Safe Operating Space for Wetlands in a Changing Climate. *Front. Ecol. Environ.* **2017**, *15*, 99–107. [CrossRef]
28. Green, A.J.; Bustamante, J.; Janss, G.F.E.; Fernández-Zamudio, R.; Díaz-Paniagua, C. Doñana Wetlands (Spain). In *The Wetland Book*; Springer: Dordrecht, The Netherlands, 2018; pp. 1123–1136.
29. Camacho, C.; Negro, J.J.; Elmberg, J.; Fox, A.D.; Nagy, S.; Pain, D.J.; Green, A.J. Groundwater Extraction Poses Extreme Threat to Doñana World Heritage Site. *Nat. Ecol. Evol.* **2022**, *6*, 654–655. [CrossRef]
30. Acreman, M.; Salathe, T. A Complex Story of Groundwater Abstraction and Ecological Threats to the Doñana National Park World Heritage Site. *Nat. Ecol. Evol.* **2022**, *6*, 1401–1402. [CrossRef]
31. Court of Justice of the European Union. EU Habitats Directive (Case C-559/19). Available online: <https://curia.europa.eu/juris/document/document.jsf?text=&docid=219133&pageIndex=0&doclang=en&mode=req&dir=&occ=first&part=1&cid=1871651> (accessed on 12 May 2025).
32. Acreman, M.; Casier, R.; Salathe, T. Evidence-Based Risk Assessment of Ecological Damage Due to Groundwater Abstraction; the Case of Doñana Natural Space, Spain. *Wetlands* **2022**, *42*, 63. [CrossRef]
33. Fisher, J.B.; Melton, F.; Middleton, E.; Hain, C.; Anderson, M.; Allen, R.; McCabe, M.F.; Hook, S.; Baldocchi, D.; Townsend, P.A.; et al. The Future of Evapotranspiration: Global Requirements for Ecosystem Functioning, Carbon and Climate Feedbacks, Agricultural Management, and Water Resources. *Water Resour. Res.* **2017**, *53*, 2618–2626. [CrossRef]
34. Melton, F.S.; Huntington, J.; Grimm, R.; Herring, J.; Hall, M.; Rollison, D.; Erickson, T.; Allen, R.; Anderson, M.; Fisher, J.B.; et al. OpenET: Filling a Critical Data Gap in Water Management for the Western United States. *JAWRA J. Am. Water Resour. Assoc.* **2022**, *58*, 971–994. [CrossRef]
35. Fisher, J.B.; Lee, B.; Purdy, A.J.; Halverson, G.H.; Dohlen, M.B.; Cawse-Nicholson, K.; Wang, A.; Anderson, R.G.; Aragon, B.; Arain, M.A.; et al. ECOSTRESS: NASA's Next Generation Mission to Measure Evapotranspiration From the International Space Station. *Water Resour. Res.* **2020**, *56*, e2019WR026058. [CrossRef]
36. Talsma, C.J.; Good, S.P.; Jimenez, C.; Martens, B.; Fisher, J.B.; Miralles, D.G.; McCabe, M.F.; Purdy, A.J. Partitioning of Evapotranspiration in Remote Sensing-Based Models. *Agric. For. Meteorol.* **2018**, *260–261*, 131–143. [CrossRef]
37. Marshall, M.; Tu, K.; Andreo, V. On Parameterizing Soil Evaporation in a Direct Remote Sensing Model of ET: PT-JPL. *Water Resour. Res.* **2020**, *56*, e2019WR026290. [CrossRef]
38. Zhang, L.; Marshall, M.; Nelson, A.; Vrieling, A. A Global Assessment of PT-JPL Soil Evaporation in Agroecosystems with Optical, Thermal, and Microwave Satellite Data. *Agric. For. Meteorol.* **2021**, *306*, 108455. [CrossRef]
39. Grayson, R.B.; Western, A.W.; Chiew, F.H.S.; Blöschl, G. Preferred States in Spatial Soil Moisture Patterns: Local and Nonlocal Controls. *Water Resour. Res.* **1997**, *33*, 2897–2908. [CrossRef]
40. Purdy, A.J.; Fisher, J.B.; Goulden, M.L.; Famiglietti, J.S. Ground Heat Flux: An Analytical Review of 6 Models Evaluated at 88 Sites and Globally. *J. Geophys. Res. Biogeosci.* **2016**, *121*, 3045–3059. [CrossRef]
41. Yao, Y.; Liang, S.; Yu, J.; Zhao, S.; Lin, Y.; Jia, K.; Zhang, X.; Cheng, J.; Xie, X.; Sun, L.; et al. Differences in Estimating Terrestrial Water Flux from Three Satellite-Based Priestley-Taylor Algorithms. *Int. J. Appl. Earth Obs. Geoinf.* **2017**, *56*, 1–12. [CrossRef]
42. Biggs, T.W.; Petropoulos, G.P.; Velpuri, N.M.; Marshall, M.; Glenn, E.P.; Nagler, P.; Messina, A. Remote Sensing of Evapotranspiration from Croplands. In *Remote Sensing of Water Resources, Disasters, and Urban Studies*; CRC Press: Boca Raton, FL, USA, 2015. [CrossRef]
43. Li, F.; Xiao, J.; Chen, J.; Ballantyne, A.; Jin, K.; Li, B.; Abraha, M.; John, R. Global Water Use Efficiency Saturation Due to Increased Vapor Pressure Deficit. *Science* **2023**, *381*, 672–677. [CrossRef]
44. García, M.; Sandholt, I.; Ceccato, P.; Ridler, M.; Mougin, E.; Kergoat, L.; Morillas, L.; Timouk, F.; Fensholt, R.; Domingo, F. Actual Evapotranspiration in Drylands Derived from In-Situ and Satellite Data: Assessing Biophysical Constraints. *Remote Sens. Environ.* **2013**, *131*, 103–118. [CrossRef]
45. Fisher, J.B.; Tu, K.P.; Baldocchi, D.D. Global Estimates of the Land–Atmosphere Water Flux Based on Monthly AVHRR and ISLSCP-II Data, Validated at 16 FLUXNET Sites. *Remote Sens. Environ.* **2008**, *112*, 901–919. [CrossRef]

46. Leuning, R.; Zhang, Y.Q.; Rajaud, A.; Cleugh, H.; Tu, K. A Simple Surface Conductance Model to Estimate Regional Evaporation Using MODIS Leaf Area Index and the Penman-Monteith Equation. *Water Resour. Res.* **2008**, *44*, W10419. [CrossRef]
47. Mu, Q.; Zhao, M.; Heinsch, F.A.; Liu, M.; Tian, H.; Running, S.W. Evaluating Water Stress Controls on Primary Production in Biogeochemical and Remote Sensing Based Models. *J. Geophys. Res. Biogeosci.* **2007**, *112*, G01012. [CrossRef]
48. Mu, Q.; Zhao, M.; Running, S.W. Improvements to a MODIS Global Terrestrial Evapotranspiration Algorithm. *Remote Sens. Environ.* **2011**, *115*, 1781–1800. [CrossRef]
49. Moyano, M.; Garcia, M.; Palacios-Orueta, A.; Tornos, L.; Fisher, J.; Fernández, N.; Recuero, L.; Juana, L. Vegetation Water Use Based on a Thermal and Optical Remote Sensing Model in the Mediterranean Region of Doñana. *Remote Sens.* **2018**, *10*, 1105. [CrossRef]
50. Fernández, N.; Paruelo, J.M.; Delibes, M. Ecosystem Functioning of Protected and Altered Mediterranean Environments: A Remote Sensing Classification in Doñana, Spain. *Remote Sens. Environ.* **2010**, *114*, 211–220. [CrossRef]
51. Tocados-Franco, E.; Berbel, J.; Expósito, A. Water Policy Implications of Perennial Expansion in the Guadalquivir River Basin (Southern Spain). *Agric. Water Manag.* **2023**, *282*, 108286. [CrossRef]
52. Martín-López, B.; García-Llorente, M.; Palomo, I.; Montes, C. The Conservation against Development Paradigm in Protected Areas: Valuation of Ecosystem Services in the Doñana Social–Ecological System (Southwestern Spain). *Ecol. Econ.* **2011**, *70*, 1481–1491. [CrossRef]
53. García-Novo, F.; Marín-Cabrera, C. *Doñana: Water and Biosphere*; Doñana 2005 Project—Confederación Hidrográfica del Guadalquivir (Guadalquivir Hydrologic Basin Authority), Spanish Ministry of the Environment: Madrid, Spain, 2006; ISBN 84-609-6326-8.
54. Manzano, M.; Custodio, E.; Montes, C.; Mediavilla, C. Groundwater Quality and Quantity Assessment through a Dedicated Monitoring Network. The Doñana Aquifer Experience (SW Spain). In *Groundwater Monitoring*; Quevauviller, P., Fouillac, A.-M., Grath, J., Ward, R., Eds.; Wiley and Sons, Ltd.: Hoboken, NJ, USA, 2009; pp. 273–287.
55. Amigo, I. Farming Bill Threatens Spain's Most Important Wetland, Scientists Say. Available online: <https://www.science.org/content/article/farming-bill-threatens-spain-s-most-important-wetland-scientists-say> (accessed on 30 May 2025).
56. Serrano, L.; Díaz-Paniagua, C.; Gómez-Rodríguez, C.; Florencio, M.; Marchand, M.-A.; Roelofs, J.G.M.; Lucassen, E.C.H.E.T. Susceptibility to Acidification of Groundwater-Dependent Wetlands Affected by Water Level Declines, and Potential Risk to an Early-Breeding Amphibian Species. *Sci. Total Environ.* **2016**, *571*, 1253–1261. [CrossRef]
57. Green, A.J.; Guardiola-Albert, C.; Bravo-Utrera, M.Á.; Bustamante, J.; Camacho, A.; Camacho, C.; Contreras-Arribas, E.; Espinar, J.L.; Gil-Gil, T.; Gomez-Mestre, I.; et al. Groundwater Abstraction Has Caused Extensive Ecological Damage to the Doñana World Heritage Site, Spain. *Wetlands* **2024**, *44*, 20. [CrossRef]
58. CHG. *Informe Del Estado De Los Acuíferos Del Entorno De Doñana. Año Hidrológico 2015–2016*; Confederación Hidrográfica del Guadalquivir: Sevilla, Spain, 2017.
59. Olías, M.; González, F.; Cerón, J.C.; Bolívar, J.P.; González-Labajo, J.; García-López, S. Water Quality and Distribution of Trace Elements in the Doñana Aquifer (SW Spain). *Environ. Geol.* **2008**, *55*, 1555–1568. [CrossRef]
60. CHG. *Plan Hidrológico de La Demarcación Hidrográfica Del Guadalquivir 2015–2021*; Anejo No3. Descripción de Usos, Demandas y Presiones; Confederación Hidrográfica del Guadalquivir: Sevilla, Spain, 2015.
61. EU. Council Directive 91/676/EEC Concerning the Protection of Waters against Pollution Caused by Nitrates from Agricultural Sources. *Off. J. L.* **1991**, *375*, 12.
62. Estévez, J.; Gavilán, P.; García-Marín, A.P. Data Validation Procedures in Agricultural Meteorology—A Prerequisite for Their Use. *Adv. Sci. Res.* **2011**, *6*, 141–146. [CrossRef]
63. JdA. Portal Ambiental de Andalucía. Available online: <http://www.juntadeandalucia.es/medioambiente/site/rediam/> (accessed on 1 June 2025).
64. Norman, J.M.; Kustas, W.P.; Humes, K.S. Source Approach for Estimating Soil and Vegetation Energy Fluxes in Observations of Directional Radiometric Surface Temperature. *Agric. For. Meteorol.* **1995**, *77*, 263–293. [CrossRef]
65. IFAPA. Estación Meteorológica de Lebrija I. Available online: <https://www.juntadeandalucia.es/agriculturaypesca/ifapa/riaweb/web/> (accessed on 10 December 2024).
66. Idso, S.B.; Jackson, R.D. Thermal Radiation from The Atmosphere. *J. Geophys. Res.* **1969**, *74*, 5397–5403. [CrossRef]
67. Parton, W.J.; Logan, J.A. A Model for Diurnal Variation in Soil and Air Temperature. *Agric. Meteorol.* **1981**, *23*, 205–216. [CrossRef]
68. García, M.; Villagarcía, L.; Contreras, S.; Domingo, F.; Puigdefábregas, J. Comparison of Three Operative Models for Estimating the Surface Water Deficit Using ASTER Reflective and Thermal Data. *Sensors* **2007**, *7*, 860–883. [CrossRef]
69. Rasmussen, M.O.; Sørensen, M.K.; Wu, B.; Yan, N.; Qin, H.; Sandholt, I. Regional-Scale Estimation of Evapotranspiration for the North China Plain Using MODIS Data and the Triangle-Approach. *Int. J. Appl. Earth Obs. Geoinf.* **2014**, *31*, 143–153. [CrossRef]
70. Jackson, R.D.; Hatfield, J.L.; Reginato, R.J.; Idso, S.B.; Pinter, P.J. Estimation of Daily Evapotranspiration from One Time-of-Day Measurements. *Agric. Water Manag.* **1983**, *7*, 351–362. [CrossRef]

71. Bisht, G.; Venturini, V.; Islam, S.; Jiang, L. Estimation of the Net Radiation Using MODIS (Moderate Resolution Imaging Spectroradiometer) Data for Clear Sky Days. *Remote Sens. Environ.* **2005**, *97*, 52–67. [\[CrossRef\]](#)
72. Iqbal, M. *An Introduction to Solar Radiation*; Academic Press: Toronto, ON, Canada, 1983.
73. Moran, M.S.; Clarke, T.R.; Inoue, Y.; Vidal, A. Estimating Crop Water Deficit Using the Relation Between Surface-Air Temperature and Spectral Vegetation Index. *Remote Sens. Environ.* **1994**, *49*, 246–263. [\[CrossRef\]](#)
74. Dabernig, M.; Mayr, G.J.; Messner, J.W.; Zeileis, A. Simultaneous Ensemble Postprocessing for Multiple Lead Times with Standardized Anomalies. *Mon. Weather. Rev.* **2017**, *145*, 2523–2531. [\[CrossRef\]](#)
75. García-Herrera, R.; Hernández, E.; Barriopedro, D.; Paredes, D.; Trigo, R.M.; Trigo, I.F.; Mendes, M.A. The Outstanding 2004/05 Drought in the Iberian Peninsula: Associated Atmospheric Circulation. *J. Hydrometeorol.* **2007**, *8*, 483–498. [\[CrossRef\]](#)
76. Ionita, M.; Tallaksen, L.M.; Kingston, D.G.; Stagge, J.H.; Laaha, G.; Van Lanen, H.A.J.; Scholz, P.; Chelcea, S.M.; Haslinger, K. The European 2015 Drought from a Climatological Perspective. *Hydrol. Earth Syst. Sci.* **2017**, *21*, 1397–1419. [\[CrossRef\]](#)
77. Drexler, J.Z.; Anderson, F.E.; Snyder, R.L. Evapotranspiration Rates and Crop Coefficients for a Restored Marsh in the Sacramento–San Joaquin Delta, California, USA. *Hydrol. Process.* **2008**, *22*, 725–735. [\[CrossRef\]](#)
78. Nagler, P.L.; Glenn, E.P.; Kim, H.; Emmerich, W.; Scott, R.L.; Huxman, T.E.; Huete, A.R. Relationship between Evapotranspiration and Precipitation Pulses in a Semiarid Rangeland Estimated by Moisture Flux Towers and MODIS Vegetation Indices. *J. Arid. Environ.* **2007**, *70*, 443–462. [\[CrossRef\]](#)
79. Díaz-Paniagua, C.; Aragonés, D. Permanent and Temporary Ponds in Doñana National Park (SW Spain) Are Threatened by Desiccation. *Limnetica* **2015**, *34*, 407–424. [\[CrossRef\]](#)
80. JdA. El Cultivo Del Arroz En Andalucía. *Secretaría General de Agricultura, Ganadería y Desarrollo Rural, España. Junta de Andalucía*. Available online: <https://www.juntadeandalucia.es/export/drupaljda/arr07121.pdf> (accessed on 8 July 2021).
81. Calder, I.R.; Rosier, P.T.W.; Prasanna, K.T.; Parameswarappa, S. Eucalyptus Water Use Greater than Rainfall Input—Possible Explanation from Southern India. *Hydrol. Earth Syst. Sci.* **1997**, *1*, 249–256. [\[CrossRef\]](#)
82. Garcia, M.; Fernandez, N.; Gonzalez-Dugo, M.P.; Delibes, M. Impact of Annual Drought on the Water and Energy Exchanges in the Doñana Region (SW Spain). In Proceedings of the Symposium Earth Observation and Water Cycle Science, Frascati, Italy, 18–20 November 2009; Volume 674.
83. Guardiola-Albert, C.; Jackson, C.R. Potential Impacts of Climate Change on Groundwater Supplies to the Doñana Wetland, Spain. *Wetlands* **2011**, *31*, 907–920. [\[CrossRef\]](#)
84. Custodio, E.; Manzano, M.; del Olmo, C.M. *Las Aguas Subterráneas En Doñana: Aspectos Ecológicos y Sociales*; Consejería de Medio Ambiente: Madrid, Spain, 2009.
85. IPCC Expert Meeting on Climate Change, Food, and Agriculture. *Meeting Report of the Intergovernmental Panel on Climate Change*; World Meteorological Organization: Geneva, Switzerland, 2015.
86. UNESCO Convention Concerning the Protection of the World Cultural and Natural Heritage. World Heritage Committee-Forty First Session. Available online: <http://whc.unesco.org/archive/2017/whc17-41com-7B-en.pdf> (accessed on 10 May 2021).

Disclaimer/Publisher’s Note: The statements, opinions and data contained in all publications are solely those of the individual author(s) and contributor(s) and not of MDPI and/or the editor(s). MDPI and/or the editor(s) disclaim responsibility for any injury to people or property resulting from any ideas, methods, instructions or products referred to in the content.